X-ray attenuation models to account for beam hardening in computed tomography

Q. Yang,[1] W.K. Fullagar,[1] G.R. Myers,[1] S.J. Latham,[1] T. Varslot,[2] A.P. Sheppard,[1] and A.M. Kingston[1,*]

[1]*Department of Applied Mathematics, Research School of Physics and Engineering, Oliphant Building 60, Mills Road, The Australian National University, Canberra Acton ACT 2601*
[2]*Thermo Fisher Scientific, Trondheim, Norway*
[*]*andrew.m.kingston@anu.edu.au*

Abstract: We introduce a beam-hardening correction method for lab-based X-ray computed tomography (CT) by modifying existing iterative tomographic reconstruction algorithms. Our method simplifies the standard Alvarez-Macovski X-ray attenuation model (Physics in Medicine & Biology, **5**, 733 [1976]) and is compatible with conventional (i.e. single-spectrum) CT scans. The sole modification involves a *polychromatic* projection operation which is equivalent to applying a weighting that more closely matches the attenuation of polychromatic X-rays. Practicality is a priority, so we only require information about the X-ray spectrum and some constants relating to material properties. No other changes to the experimental setup or the iterative algorithms are necessary. Using recontructions of simulations and several large experimental datasets, we show that this method is able to remove or reduce cupping, streaking, and other artefacts from X-ray beam hardening and improve the self-consistency of projected attenuation in CT. When the assumptions made in the simplifications are valid, the reconstructed tomogram can even be quantitative.

1. Introduction

X-ray computed tomography (XCT) is a versatile tool in widespread use that produces 3D volume information non-destructively [1, 2]. The 3D volume (or tomogram), which maps the spatial distribution of the X-ray attenuation coefficients in the object, is reconstructed from the measured set of 2D radiographs (or projections). However, the quality of XCT tomograms are often degraded by artefacts, a major example being *beam-hardening* artefacts [3–5]. In lab-based XCT, the X-rays are polychromatic, i.e. the X-ray beam contains X-ray photons of different energies. The polychromatic X-rays produced by lab sources *harden* (i.e. their mean energy becomes higher) as they pass through attenuating materials, because the *soft* (i.e. low-energy) X-rays are preferentially attenuated [6]. Common reconstruction algorithms such as Filtered back-projection [7] and the Simultaneous Iterative Reconstruction Technique (SIRT) [8] assume no such change in the X-ray spectrum, since the mathematical model which underpin these algorithms is only valid for monochromatic X-rays without scatter. It is therefore not surprising that artefacts appear in the tomographic reconstructions for experiments which use polychromatic X-rays. For example, in Fig. 1, two types of artefacts are visible: cupping raises the attenuation around the edges of the object; streaking smears the attenuation values of objects into the region between them.

The artefacts that appear in a tomogram due to X-ray beam hardening can limit its utility for non-destructive evaluation and analysis. Ideally, each tomogram voxel should take the value of the attenuation coefficient of the material in that voxel. However, beam-hardening alters the attenuation coefficients so that features in the reconstruction no longer correspond to what is present in the object. For example, in dental X-rays, the cupping effects of beam hardening may be indistinguishable from the change in natural mineral concentration in teeth enamel [9].
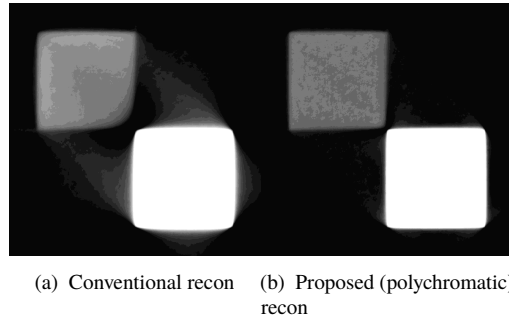
(a) Conventional recon   (b) Proposed (polychromatic) recon

Fig. 1. Reconstruction of simulated data for square beams of aluminium (left) and marble (right), both 0.2×0.2mm in size. The simulated projection data were generated using X-rays from a Tungsten target with 100keV accelerating voltage and no filtering. The tomograms have been reconstructed with 10 iterations of (a) conventional ordered subset SIRT; (b) ordered subset SIRT modified with our proposed polychromatic method.

This effect is more pronounced in applications involving quantitative analysis or classification of materials. For example, in geological samples, feldspar would be wrongly classified as quartz at the edge of the sample due to cupping [10]. Removing beam-hardening artefacts is essential for accurate analysis in these scenarios.

There are hardware and software approaches that deal with beam-hardening artefacts. The principle hardware approach in the lab is filtering, where the X-ray beam is attenuated or *pre-hardened*. This reduces the proportion of soft X-rays in the illuminating beam, which then has less potential to *harden* as it passes through the sample [11]. However, filtering comes at the cost of decreased flux and signal-to-noise ratio (SNR) in the raw measured data.

Linearisation is a simple and commonly used software correction method. This involves remapping the measured attenuation of polychromatic X-rays into an equivalent attenuation of monochromatic X-rays by linearising the total-attenuation/thickness relation of the material [12–14]. Linearisation does not address the cause of beam hardening and only deals with the symptoms, since it directly modifies the experimental data. If the object consists of a single material, linearisation can accurately compensate for beam hardening and requires only one calibration scan (typically with a wedge of the material to produce the linear relations, e.g. [15]). The attenuation component can also be approximated by joining two lines together, their gradients depend on the distance the beam has travelled in the object [16]. For multi-material objects, this calibration, with additional Segmentation and estimation of the path-length, is required for each material, since they all have unique attenuation-distance curves [17]. For two materials, this can be avoided by assuming the lower attenuating material has zero attenuation [18]. Nevertheless, it is common to choose a single curve to correct the entire dataset even if the correction is only approximate (e.g. [13]). In general, linearisation is complicated and less effective for the multi-material case since beam-hardening artefacts make both segmentation and path-length estimation unreliable.

Dual-energy CT methods have both software and hardware components. It involves taking two complete XCT scans of the sample with different X-ray spectra and using the additional information to solve for the two independent components of the material attenuation coefficients [19–21]. Because they incorporate polychromatic models in the reconstruction algorithm itself, they deal with the cause of the issue. The Alvarez-Macovski (AM) model is the usual model for X-ray attenuation in dual-energy XCT. It describes X-ray attenuation as the sum of photoelectric effect and Compton (or inelastic) scattering [19]. The AM model approximates the attenuation

of low atomic number materials reasonably well, but is limited for heavier elements since it does not account for the discontinuities in X-ray attenuation at material absorption edges. The photoelectric absorption and Compton scattering changes differently with energy, but the two scans provide sufficient information to solve for the magnitude of each effect and therefore generate corrected tomographic reconstructions. Unfortunately, dual-energy methods require either expensive energy-resolving detectors or longer acquisition time and dose.

Recent iterative software methods, such as [22, 23], try to incorporate a correction method inside the iterative tomographic reconstruction algorithm. De Man et al. in [22] adapts the AM two component model inside a maximum-likelihood for transmission tomography (ML-TR) algorithm [24]. The resulting corrected reconstruction is a natural consequence of the physics, and no more details need to be supplied. However, this method has a high computational cost. Another method with similar high computational cost was presented by van Gompel et al., which uses gradient based optimisation to segment the object into different materials, and then fit the parameters of the AM two component AM model before carrying out each iteration in the reconstruction algorithm [25]. If the materials are known, then the decomposition and reconstruction can happen in one step, with no need for the AM model, for example [26]. However, this method is less suitable when the composition of the reconstruction is unknown. Unsurprisingly, iterative methods incorporating beam-hardening correction have not yet entered widespread use since iterative methods themselves have only recently become practical due to increased computational power. The additional complexity introduced by the correction schemes makes them even less accessible to general users of XCT. A common method to simplify the attenuation model is to ignore Compton scattering and consider only the photoelectric absorption mechanism of attenuation (e.g., [27]). Here we explore several other simplifications as well that may be more appropriate in certain scenarios.

We present a beam-hardening correction method that integrates with any conventional iterative tomographic reconstruction algorithm and still solves the cause of the issue. Given the X-ray spectrum used in the experiment, we modify the forward-projection operation to yield a polychromatic model of X-ray attenuation. Using this accurate forward model, we can more closely approximate the actual attenuation process involved in experiments using polychromatic X-rays and account for beam hardening. The results are tomograms that have reduced artefacts and, when the assumptions are valid, voxel gray-scale values that match attenuation coefficients. Like De Man et al. we incorporate simplifications of the AM model as the basis of our polychromatic model [22]. However, our focus is to ensure it is practical to implement and deploy in production environments.

The remainder of the paper proceeds as follows: In Sect. 2 we outline the general concept of our proposed method, the various assumptions required and simplifications made to the AM model. The implementation of the suite of methods developed are outlined in Sect. 2.3. The performance is first demonstrated using simulated results in Sect. 3, then applied to several experimental CT datasets in Sect. 4. Some concluding remarks are included in Sect. 5 along with an outline of potential future research directions.

2. Developing a polychromatic projection operator to model X-ray beam hardening

The root cause of beam hardening artefacts in XCT is the discrepancy between the monochromatic X-ray model used in reconstruction and the physical polychromatic X-rays illuminating the sample. Therefore we require an iterative reconstruction algorithm which models the polychromatic projection process that occurs during the experiment.

In this section we assume general familiarity of XCT iterative reconstruction algorithms on discrete data, and deal only with the modification we made to the projection operation. We start with a model of polychromatic attenuation, and follow general conventions in notation [8, 28–30].

Projected attenuation $\hat{y}$ ("ˆ" denoting simulated rather than measured quantities) is approximated by the projection operator

$$\hat{y}_{i,k} = \sum_j A_{ij}\mu_{j,k},\tag{1}$$

where $\mu_{j,k}$ is the energy-dependent linear attenuation coefficients for pixel j (in the reconstruction/volume space) at some discretised energy bin k, and A_{ij} is the matrix representing the projection operation.

The measured data $I_{i,k}$ is the detected illumination intensity at the ith detector pixel at energy bin k after it has passed through the object. Since the X-ray has a spectrum we let S_k be the normalised spectral intensity, and $I_{i,0}$ the total incident illumination intensity across all energies. The intensity of the X-ray beam in the kth energy bin that strikes detector pixel i without the attenuating object would be $S_k I_{i,0}$. Consequently, we define the *measured attenuation* as $y_{i,k} \equiv -\log(I_{i,k}/(S_k I_{i,0}))$.

The simulated projected attenuation can be used to predict the ith simulated intensity transmitted by the object. This is done by applying the the Beer-Lambert law at each energy bin k [31]

$$\hat{I}_{i,k} = S_k I_{i,0} \exp\left(-\hat{y}_{i,k}\right).\tag{2}$$

The spectral density S_k can either be measured empirically or calculated from a model of the spectrum. To compare the simulated and measured attenuations, we divide both sides of equation (2) by $I_{i,0}$ and take the logarithm. In conventional iterative reconstruction algorithms a single energy bin is used to describe the CT scanning process. In this monochromatic case, $S_k = \sum_k \delta(x, k_0) y_{i,k} = \hat{y}_{i,k_0}$ for some energy bin k_0. In this paper we replace this approximation with a *polychromatic projection operator* (equation (3)) that uses a more complete model which sums across multiple energy bins

$$\hat{y}_i \equiv -\log\left[\sum_k S_k \exp\left(-\sum_j A_{ij}\mu_{j,k}\right)\right].\tag{3}$$

The polychromatic projection operator in equation 3 is potentially impractical, requiring a projection operation at each energy bin, unless some approximation is used to simplify the calculation of $\sum_j A_{ij}\mu_{j,k}$. We also need the energy dependence of μ to generate the attenuation coefficients $\mu_{j,k}$ at the k different energies. To overcome this we have employed the Alvarez-Macovski model.

2.1. The Alvarez-Macovski model

The Alvarez-Macovski (AM) model significantly reduces the number of degrees of freedom in the linear attenuation coefficients $\mu_{j,k}$, and is our starting point for simplifying equation 3. The AM model describes X-ray attenuation using the photoelectric effect, Φ, and Compton scattering, Θ [19]. These components can be modelled as functions of atomic number (Z), density (ρ) and atomic weight (A) as follows:

$$\begin{aligned}\mu_{j,k} &= \Phi_{j,k} + \Theta_{j,k} \\ &= \frac{Z_j}{A_j}\rho_j\left(K_\Phi Z_j^{n-1} \cdot \frac{1}{E_k^m} + K_\Theta f_{\text{KN}}(E_k)\right).\end{aligned}\tag{4}$$

Here f_{KN} is the Klein-Nishina function, which is the scattering cross section (probability) of X-ray photons by electrons, and is a result derived in quantum mechanics [32]. We usually approximate Z/A by 0.5, and the exponents used are $m = 3$ and $n = 4.2$ as calibrated in [33]. K_Φ and K_Θ are constants of proportionality. Since the model does not capture absorption edge

transitions, the value of these constants depends on the spectrum used and the materials present. We chose the values for K_Φ and K_Θ which minimise the spectrally-weighted, relative L^2 residual of the AM model from the National Institute of Standards and Technology XCOM attenuation database (NIST-XCOM) [34] for each material present in the reconstruction. This is not possible for reconstruction of objects containing unknown material, but since the values for most common objects with atomic number up to tin (50) are 23-25 for K_Φ and 0.3-0.49 for K_Θ, we don't anticipate any major difficulty in selecting an optimal value that would suit most materials in this range.

We observe that the Alvarez-Macovski equation does not account for absorption-edges of materials, however, it is a useful attenuation model for most common materials for two reasons: 1) K-edges of common materials (including metals) fall below the typical energy range of imaging spectra; 2) the general shape of the attenuation curve provided by the AM model is sufficient to deliver substantially improved reconstruction quality even if it is not quantitative for some metals.

2.2. Proposed simplifications of the AM model

The AM model has reduced energy dependence of X-ray attenuation $\mu_{j,k}$ down to two independent variables: Z_j and ρ_j. However, in single-energy imaging we only have a single equation per voxel j, so a further assumption is required to reduce the model to a single variable. We propose several simple assumptions for condensed matter:

$$\alpha_0 Z + \alpha_1 \rho + \alpha_2 = 0. \tag{5}$$

The values taken by the coefficients α_0, α_1 and α_2 determine which of the several assumptions applies; each corresponds to a plausible physical scenario. We can obtain five basic simplifications by setting the coefficients as follows:

I $\alpha_2 = 0, \alpha_0 \to 0, \rho \to 0$: μ comprised of Φ only

II $\alpha_2 = 0, \alpha_1 \to 0, Z \to 0$: μ comprised of Θ only

III $\alpha_2 = 0$: Z is proportional to ρ, i.e. $Z = c\rho$

IV $\alpha_1 = 0$: Z is constant, i.e., $Z = Z_0$

V $\alpha_0 = 0$: ρ is constant, i.e., $\rho = \rho_0$

Scenarios I and II use only one component of the AM model. The first assumption, photoelectric absorption only, is vastly more useful than the latter since f_{KN} is a slowly varying function at X-ray energy ranges so Compton scattering usually makes a smaller contribution to BH. Assumption I is very suitable for relatively high attenuation materials such as iron/steel where the photoelectric attenuation equals Compton scatter only at around $100 keV$.

Scenario III assumes that for all the material, the density is proportional to the atomic number. This is the most general assumption since the ratio, c, of a large number of condensed matter falls in $3 < c < 8$.

Scenario IV assumes that all materials (void excepted) have the same atomic number. This may be useful in more specific cases where, for example, for a single-mineral object with sub-voxel resolution porosity, or when a contrast agent is used to help X-ray visibility of a fluid but does not change the density of the fluid perceptibly.

Scenario V assumes that all materials (void excepted) have the same density. Many materials share a similar density so this assumption is useful in scenarios such as mixtures of metals in alloys, and for mineral analysis of homogeneous geological samples. This assumption is violated by sub-resolution voids so is unlikely to be successful for porous samples with sub-resolution porosity.

2.3. Implementation considerations

Our iterative algorithm reconstructs attenuation coefficients, μ_{j,k_0}, at a specific X-ray energy E_{k_0} (usually the mean energy of the spectrum). The attenuation coefficients for each assumption (Photoelectric effect only $\mu_{j,k}^{\text{pe}}$; Compton scattering only $\mu_{j,k}^{\text{co}}$; density proportional to atomic number $\mu_{j,k}^{\text{prop}}$; constant atomic number $\mu_{j,k}^{\text{ca}}$; constant density $\mu_{j,k}^{\text{cd}}$) are given by the following simplification of the AM model:

$$\mu_{j,k}^{\text{pe}} = \frac{1}{2}K_{\Phi}\rho_j Z_j^{3.2} \cdot \frac{1}{E_k^3} \tag{6}$$

$$\mu_{j,k}^{\text{co}} = \frac{1}{2}K_{\Theta}\rho_j f_{\text{KN}}(E_k) \tag{7}$$

$$\mu_{j,k}^{\text{prop}} = \frac{Z_j}{2c}\left(K_{\Phi}Z_j^{3.2} \cdot \frac{1}{E_k^3} + K_{\Theta}f_{\text{KN}}(E_k)\right) \tag{8}$$

$$\mu_{j,k}^{\text{ca}} = \frac{1}{2}\rho_j\left(K_{\Phi}Z_0^{3.2} \cdot \frac{1}{E_k^3} + K_{\Theta}f_{\text{KN}}(E_k)\right) \tag{9}$$

$$\mu_{j,k}^{\text{cd}} = \frac{1}{2}\rho_0\left(K_{\Phi}Z_j^{3.2} \cdot \frac{1}{E_k^3} + K_{\Theta}f_{\text{KN}}(E_k)\right) \tag{10}$$

These simplifications allow us to generate the projected attenuation at different energies E_k from a single tomogram of μ_{j,k_0}.

2.3.1. Photoelectric absorption only

For this assumption (simplification I), μ_{j,k_0} is projected, (i.e., $\hat{y}_{j,k_0} = \sum_j a_{ij}\mu_{j,k_0}$), and the projected attenuation at the different energies E_k are obtained by scaling:

$$\begin{aligned}
\sum_j a_{ij}\mu_{j,k}^{\text{pe}} &= \sum_j a_{ij}\frac{1}{2}K_{\Phi}\rho_j Z_j^{3.2} \cdot \frac{1}{E_k^3} \\
&= \frac{E_{k_0}^3}{E_k^3} \cdot \sum_j a_{ij}\frac{1}{2}K_{\Phi}\rho_j Z_j^{3.2} \cdot \frac{1}{E_{k_0}^3} \\
&= \frac{E_{k_0}^3}{E_k^3} \cdot \sum_j a_{ij}\mu_{j,k_0}
\end{aligned}$$

2.3.2. Compton scattering only

This assumption (simplification II) is similar to the photoelectric effect only assumption: we carry out one projection operation, and then scale according to the Klein-Nishina function $f_{KN}(E_k)$.

$$\sum_j a_{ij}\mu_{j,k}^{\text{co}} = \frac{f_{KN}(k)}{f_{KN}(k_0)} \cdot \sum_j a_{ij}\mu_{j,k_0}$$

2.3.3. Z Proportional to ρ

For this assumption (simplification III), we first solve for Z_j from $\mu_{j,k}^{\text{prop}}$ using equation (8). This can be performed in a variety of ways, including numerical methods such as Newton-Raphson. Once the value of Z_j has been recovered, ρ_j can be calculated from $\rho_j = Z_j/c$.

Once we have the values for both ρ_j and Z_j, we can then project both ρ and Z separately, because each component of the X-ray attenuation model scales differently according to energy.

We must have two sparate projections in order to generate the different projected attenuations at the k different energies:

$$\sum_j a_{ij}\mu_{j,k}^{\text{prop}} = \sum_j a_{ij}\frac{1}{2c}\left(K_\Phi Z_j^{4.2}\cdot\frac{1}{E_k^3} + K_\Theta Z_j f_{\text{KN}}(k)\right)$$

$$= \frac{1}{2c}\left(K_\Phi \sum_j a_{ij}Z_j^{4.2}\cdot\frac{1}{E_k^3} + K_\Theta \sum_j a_{ij}Z_j f_{\text{KN}}(E_k)\right)$$

$$= \frac{E_{k_0}^3}{E_k^3}\cdot\sum_j a_{ij}\left(\frac{1}{2c}K_\Phi Z_j^{4.2}\cdot\frac{1}{E_{k_0}^3}\right) +$$

$$\frac{f_{\text{KN}}(E_k)}{f_{\text{KN}}(E_{k_0})}\sum_j a_{ij}\left(\frac{1}{2c}K_\Theta Z_j\cdot f_{\text{KN}}(E_{k_0})\right)$$

$$= \frac{E_{k_0}^3}{E_k^3}\sum_j a_{ij}\mu_{j,k_0}^{\text{pe}} + \frac{f_{\text{KN}}(E_k)}{f_{\text{KN}}(E_{k_0})}\sum_j a_{ij}\mu_{j,k_0}^{\text{co}}$$

2.3.4. Atomic number is constant

For this assumption (simplification IV), we solve equation (9) for ρ_j given that atomic number Z_0 is a constant:

$$\rho_j = \frac{2\mu_{j,k}^{\text{ca}}}{K_\Phi Z_0^{3.2}\cdot\frac{1}{E_k^3} + K_\Theta f_{\text{KN}}(E_k)}. \tag{11}$$

Given Z_0, and knowing ρ_j, we can then project the density and and scale it:

$$\sum_j a_{ij}\mu_{j,k}^{\text{ca}} = \frac{E_{k_0}^3}{E_k^3}\cdot\frac{1}{2}K_\Phi \sum_j a_{ij}\rho_j Z_0^{3.2}\cdot\frac{1}{E_{k_0}^3} +$$

$$\frac{f_{\text{KN}}(E_k)}{f_{\text{KN}}(E_{k_0})}\frac{1}{2}K_\Theta \sum_j a_{ij}\rho_j\cdot f_{\text{KN}}(E_{k_0})$$

$$= \frac{1}{2}\sum_j a_{ij}\rho_j\left(K_\Phi Z_0^{3.2}\frac{E_{k_0}^3}{E_k^3} + K_\Theta\frac{f_{\text{KN}}(E_k)}{f_{\text{KN}}(E_{k_0})}\right)$$

2.3.5. Density is constant

For this assumption (simplification V), we solve for Z_j using the equation:

$$Z_j = \sqrt[3.2]{\frac{E_{k_0}^3}{K_\Phi}\left(\frac{2}{\rho_0}\mu_{j,k}^{\text{cd}} - K_\Theta f_{\text{KN}}(E_k)\right)}. \tag{12}$$

Given ρ_0, and knowing Z_j, we can project the two components of the AM model separately and scale as follows:

$$\sum_j a_{ij}\mu_{j,k}^{\text{cd}} = \frac{E_{k_0}^3}{E_k^3} \cdot \frac{1}{2}K_\Phi \sum_j a_{ij}\rho_0 Z_j^{3.2} \cdot \frac{1}{E_{k_0}^3} +$$

$$\frac{f_{\text{KN}}(E_k)}{f_{\text{KN}}(E_{k_0})}\frac{1}{2}K_\Theta \sum_j a_{ij}\chi_j\rho_0 \cdot f_{\text{KN}}(E_{k_0})$$

$$= \frac{E_{k_0}^3}{E_k^3} \sum_j a_{ij}\mu_{j,k_0}^{\text{pe}} + \frac{f_{\text{KN}}(E_k)}{f_{\text{KN}}(E_{k_0})} \sum_j a_{ij}\mu_{j,k_0}^{\text{co}}.$$

Where χ_j is a characteristic function of the atomic number $\chi_j = 1$ where $Z_j \geq 1$, otherwise $\chi_j = 0$.

2.3.6. Discussion

We note that simplifications I and II only use one component of the AM model and thus require only one forward projection for each iteration. Similarly, simplification IV also require only one projection. Simplifications III and V use the full model, they are slower since they need two forward projections per iteration.

Once we have generated the projected attenuations, $\sum_j a_{ij}\mu_{j,k}$, at the k different energies, these are combined with the X-ray spectrum via equation (3) to give the measured polychromatic projected attenuation $\hat{y}_i$. The rest of the iterative reconstruction algorithm proceeds normally with the monochromatic back-projection operation.

If only one forward projection is used per iteration, our reconstruction method takes about same time per iteration when compared to the conventional reconstruction, otherwise when two forward projections are necessary, time per iteration is increased by about 40%.

The adjoint operator for polychromatic forward-projection, if it exists, is complex and requires multiple back-projections. In the interest of speed and simplicity we assume that the residual in the projection data is at energy E_{k_0} and the backprojected update to the volume is also at energy E_{k_0}. We expect this compatibility to improve as the iterations proceed and therefore our assumptions in section 2.3 remain valid. since we do not use an adjoint operation for the back-projection, our method is not guaranteed to converge. However, we expect that it will approach the same result as that when using with a polychromatic back-projection operator but with a slower convergence rate.

The tomographic reconstruction is performed at a specific energy, E_{k_0}. The selection of E_{k_0} mainly affects the convergence per iteration of the iterative reconstruction algorithm. We suggest E_{k_0} be chosen as the weighted average of the spectral density; this is the energy which most closely approximates the monochromatic backprojection operation. Due to the large change in X-ray attenuation values with energy (See Fig. **??**), our scheme becomes unstable with extreme values of E_{k_0}.

Since we are reconstructing the attenuation coefficients at a specific energy, we can use our simplifications to solve the Alvarez-Macovski equation on the tomogram and extract the density or atomic number information for each pixel, therefore when the assumptions are valid our reconstruction is indeed quantitative.

3. Simulated demonstrations

These simulations are designed to test the accuracy of the AM model and the simplification schemes across a range of different materials. We demonstrate both the qualitative aspects in terms of the visibility of the streaks and cupping and the quantitative aspects in terms of

how well the reconstructed attenuation values match those from the NIST-XCOM attenuation database [34].

3.1. Simulation Methods

3.1.1. Generating the Simulated Intensities

The simulated phantom of a 2D image is generated using the procedure described in Fig. 3. The attenuation data for each material are taken from the NIST-XCOM database [34]. The spectrum (Figure 2) is generated using a model that includes X-ray generation via Brehmstrahlung (Kramer's Law) and characteristic emission from a tungsten target; attenuation en route to the detector; and detector efficiency [33]. We assume the spectrum was detected by a perfect energy-integrating scintillation detector with the same spefications as the one used in the experiments (See Section 4). Our model accounts for spectral response of the detector. However, other effects such as partial detection and electronic noise are not included. The resolution of the spectrum model is 1 keV.
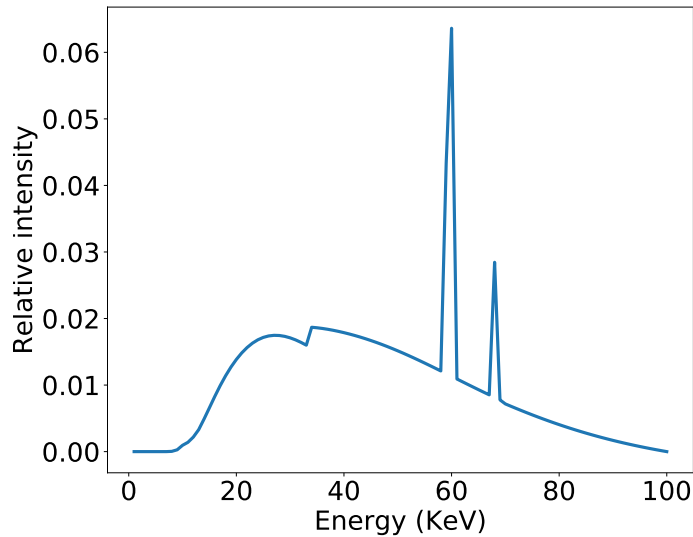

Fig. 2. The spectrum used in the simulation, as seen by the detector. Spectrum was simulated from an X-ray source with a tungsten target, an accelerating voltage of 100keV and no additional filters. The detector is 700μm of CsI scintillator.

We have selected relatively common materials in the simulation and experiments so that each material fulfills one of the assumptions in section 2.2; together these materials test every assumption apart from the Compton scattering only assumption, which doesn't beam-hardening anyway. For the simulations, the first pair is used to test simplification IV and the second pair is used to test simplification V.

The first sample (Sample 1) consists of a vaterite block and an aragonite block. The minerals are $CaCO_3$ with different crystalline packing and therefore different densities, but the same effective atomic number. The blocks have a square cross-section with side length 1mm. The second sample (Sample 2) consists of bone and a contrast dye. Again both materials have a square cross-section with side length 1mm. The material properties of these samples are presented in Table 1. The input sample data share the following properties: 2D images with resolution of
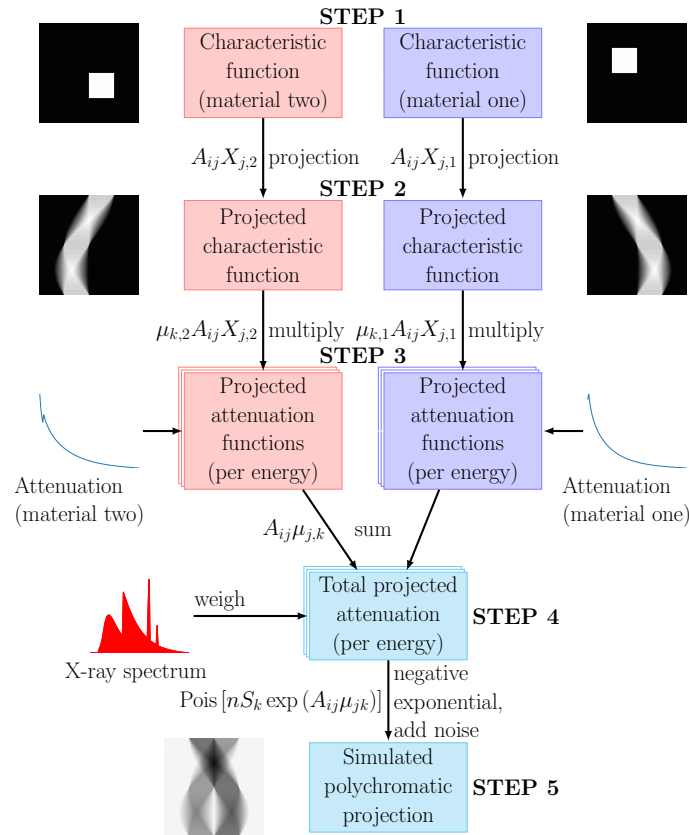
Fig. 3. Generating the simulated phantom. 1. The location of each material is given by a characteristic function (1 where the sample is present, 0 otherwise). 2. The characteristic function is projected to give the unit projected attenuation. 3. Each projected characteristic function is multiplied by the attenuation coefficient at each X-ray energy, material density, and pixel pitch to obtain the total attenuation at each energy for that material. 4. For each energy, the total attenuations for each material are added together, then converted to transmission by applying the negative exponential. This gives the transmission of the X-ray beam through all materials of the object at each energy. 5. The transmission data at each energy are weighted by the photon-count spectrum and Poisson noise (simulating photon shot-noise) is added to each energy bin separately. The resulting data at each energy are scaled by photon energy and summed to give the total transmitted intensity.

1000×1000 pixels with a pixel pitch of 0.2μm. The X-ray spectrum was simulated with an accelerating voltage of 100keV and no additional filters.

Table 1. Physical properties of the materials used in simulations and experiments. Density ρ, effective atomic number Z_{eff} [33], and their ratio.

Material	ρ (g cm^{-3})	Z_{eff}	Z/ρ
Vaterite	2.54	15.34	6.04
Aragonite	2.93	15.34	5.24
Bone	1.90	18.0	9.53
Contrast	1.0	9.55	9.53
Titanium alloy	4.54	22	4.85
Aluminium	2.7	13	4.81
Marble	2.7	16	5.90

The sinograms are generated using a parallel beam geometry with 1000 angles uniformly distributed over 180°. We have used a 1D detector with 1000 elements/pixels per measurement with a pixel pitch of 0.2μm, (matching the resolution of the sample images). Poisson noise was added while converting the sinograms to measured intensity.

3.1.2. Reconstruction of the Simulated data

We modified the ML-TR iterative reconstruction algorithm presented in [24] to include the proposed polychromatic projection operation. Iterative tomographic reconstruction was performed both with and without our modifications for comparison. Convergence was accelerated by employing both ordered-subsets and multigrid methods: Ten iterations were performed at one-quarter the original scale; the result is upsampled and used as a seed for six iterations at half the original scale; the result is upsampled once again and seeds four iterations at full resolution. If only one forward projection is used per iteration, our reconstruction method takes about same time per iteration when compared to the conventional reconstruction, otherwise when two forward projections are necessary, time per iteration is increased by about 40%. For reconstruction that require the X-ray spectrum, the same spectrum which generated the sinogram is used. This is partly due to convenience, and partly because the increase in spectral resolution poses no significant computational costs in either obtaining the spectrum or the reconstruction. Nevertheless, we tested the use of spectra with 2keV, 5keV or 10keV bins by summing together spectral densities in adjacent 1keV bins. We observed less than 2% difference in the mean reconstructed attenuation values when using 1KeV bins compared to 10KeV bins.

3.2. Simulation Results

The results of the tomographic reconstruction of sample 1 (vaterite and aragonite) using simplification IV (constant atomic number) are shown in Fig. 4. The results for sample 2 (bone and contrast dye) using simplification III (density is proportional to atomic number) are shown in Fig. 5.

(a) Conventional recon   (b) Profile (conventional)

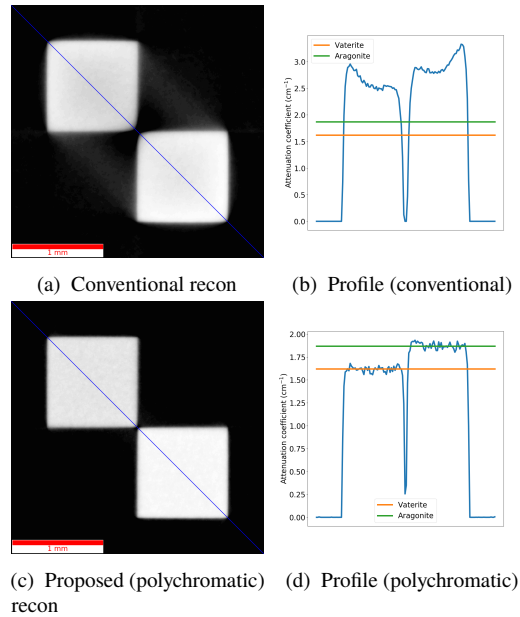(c) Proposed (polychromatic)   (d) Profile (polychromatic)
recon

Fig. 4. Reconstruction of simulated polychromatic projections of vaterite and aragonite at 46keV. Top left mineral: vaterite; Lower right mineral: aragonite. The left hand column shows the reconstructed image, the right hand column shows the line profile through the blue line marked in the images. Row 1: conventional recon; Row 2: proposed (polychromatic) recon (simplification IV). The expected attenuation (NIST-XCOM attenuation values at 46keV) is given as the orange and green lines in the line profile.

3.3. Simulation Analysis and Discussion

In the reconstructed image for the reconstruction of sample 1 (Fig. 4), beam-hardening artefacts are reduced when the polychromatic spectrum is incorporated. In the reconstructed image (Fig. 4c and Fig. 4a), the streaks between the two minerals are eliminated and there is much greater consistency of the attenuation coefficient value within each material. In the profile plot, the cupping effect (concavity of the curve in Fig. 4b) is completely eliminated in the reconstructed data using the polychromatic spectrum (Fig. 4d). We also note that the values in the profile of the corrected image match the NIST-XCOM attenuation coefficient values at the reconstruction energy of 46keV; this NIST-XCOM data was used to generate the simulations. The profile for the uncorrected reconstruction (Fig. 4b) on the other hand show no such resemblance. Our proposed method is able to achieve quantitative reconstruction.

Similarly for the reconstruction of sample 2, we observe reduced artefacts directly from the reconstructed image (Fig. 5c and Fig. 5a) in the form of reduced cupping and better defined contour of the boxes. The degree of correction of this cupping is more prominent in the profile plots (Fig. 5d and Fig. 5b). The attenuation coefficient of the two materials recovered at the reconstruction energy of 46keV also correspond to the expected values in the NIST-XCOM data. The contrast dye falls slightly below the expected value. This is due to the AM model underestimating the attenuation due to the presence of an absorption edge in the NIST-XCOM data.

(a) Conventional recon   (b) Profile (conventional)

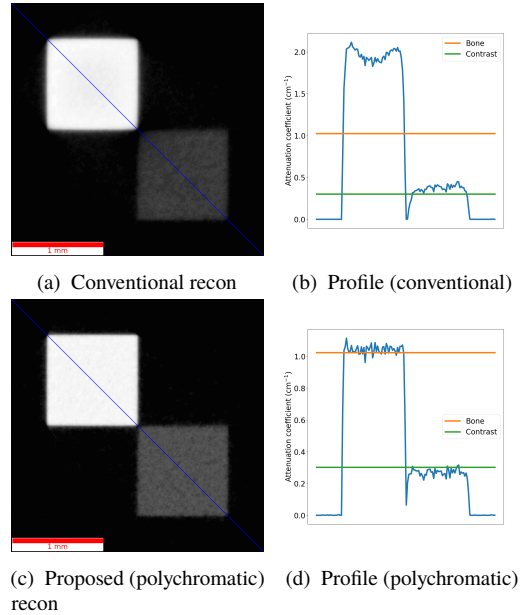(c) Proposed (polychromatic) recon   (d) Profile (polychromatic)

Fig. 5. Reconstruction of simulated polychromatic projections of bone and contrast dye at 46keV. Top left material: water with contrast dye; Lower right material: bone. The left hand column shows the reconstructed image, the right hand column shows the line profile through the blue line marked in the images. Row 1: conventional recon; Row 2: proposed (polychromatic) recon (simplification III). The expected attenuation (NIST-XCOM attenuation values at 46keV) is given as the orange and green lines in the line profile.

4. Experimental Demonstrations

4.1. Experimental Methods

Simple objects composed of different materials were imaged with the Heliscan XCT system at ANU CTLab. This system uses a fine-focus geometry with a Hamamatsu micro-focus X-ray source employing a tungsten target in transmission mode. Detectors used at the facility are amorphous silicon Flat-Panels with a CsI scintillator. The detector specifics (pixel array dimensions and pixel pitch, P) are given (per object) below. The sample manipulator can rotate the object and translate the object along the rotation axis enabling circular, helical, and more complex X-ray source trajectories about the sample. The detector is typical set at distances $300 < L < 600$mm from the X-ray source and magnification of L/R is achieved through the cone-beam geometry with the rotation axis at distance Rmm.

The first object was composed of two rods: a 10.4mm diameter rod composed of marble ($CaCO_3$) and a 8.2mm diameter rod composed of Aluminium (Al). It was scanned at a distance $R = 40$mm from the X-ray source, with the detector at $L = 316$mm, using a spectrum generated with a 120kV accelerating voltage and filtered by 0.1mm of Al. The detector utilised was a Varian 4030 Flat Panel detector with a 2048×1536 pixel array and pixel pitch $P = 139 \mu$m.

The second object was a column of Titanium alloy (Ti6Al6V) produced by an additive manufacturing system. It has an approximate diameter of 0.2mm and a length of 1.1mm. It was scanned at a distance $R = 1.0$mm from the X-ray source, with the detector at $L = 601$mm, using a spectrum generated with a 100kV accelerating voltage and no filtering. The detector utilised was a Perkin Elmer Flat Panel detector with a 2048×2048 pixel array and pixel pitch $P = 200 \mu$m.

The scans were carried out using space-filling trajectories (as described in [35]) over the course of several hours. Tomographic reconstruction was performed using 16 iterations of ordered subset ML-TR within the Mango software suite developed at the CTLab [36, 37].

The forward projection operation in the Mango software was modified to incorporate a polychromatic model using the simplifications given in section 2.2. This is the only substantial change required for the iterative tomographic reconstruction software to account for beam hardening. Note that this modification is suitable for any iterative algorithm that uses the same projection operator, e.g., it was also successfully tested on the experimental data using a SIRT algorithm.

4.2. Experimental Results

Horizontal slices through the tomographic volumes of aluminium (bottom) and marble (top) rods reconstructed assuming monochromatic and polychromatic X rays are given in Fig. **??**. Profiles of the data are also provided. The modified reconstruction algorithm (Fig. 6c-6d) has assumed constant density (simplification V) with $\rho = 2.7 \text{g cm}^{-3}$. We used the same X-ray spectrum model from section 3.1.1 with 1keV bins. This is a simple spectrum model (as described in [33]) and calibrated using measurements with a spectrum analyser (XR-100T-CdTe Amptek detector). The measured spectra were remapped from a 1mm CdTe detector to assume a $700\mu m$ CsI scintillator before model calibration.

(a) Conventional recon

(b) Profile (conventional)

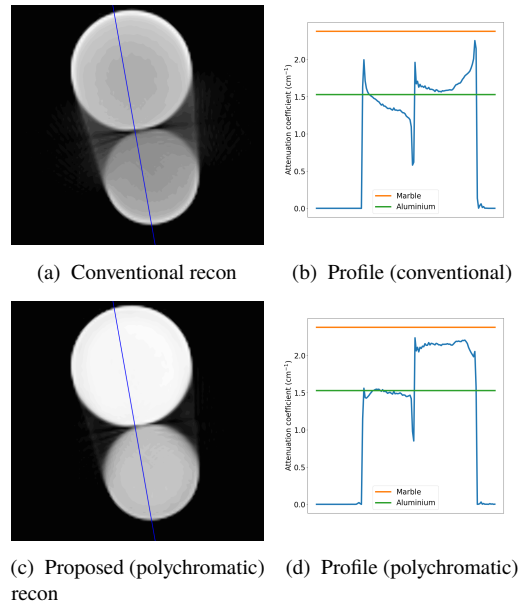(c) Proposed (polychromatic) recon

(d) Profile (polychromatic)

Fig. 6. Horizontal slices through the 3D tomographic reconstruction of experimental data for marble and aluminium rods at 46keV. The left hand column shows the reconstructed image, the right hand column shows the line profile through the blue line marked in the images. Row 1: conventional recon; Row 2: proposed (polychromatic) recon (simplification V). The expected attenuation (NIST-XCOM attenuation values at 46keV) is given as the orange and green lines in the line profile.

Horizontal slices through the tomographic volumes of the printed titanium column reconstructed assuming monochromatic and polychromatic X rays are given in Fig. 7. Profiles of the data are also provided. The modified reconstruction algorithm (Fig. 7c-7d) has assumed that attenuation is dominated by photoelectric absorption (simplification I). The spectrum used has 1keV bins.

(a) Conventional recon   (b) Profile (conventional)

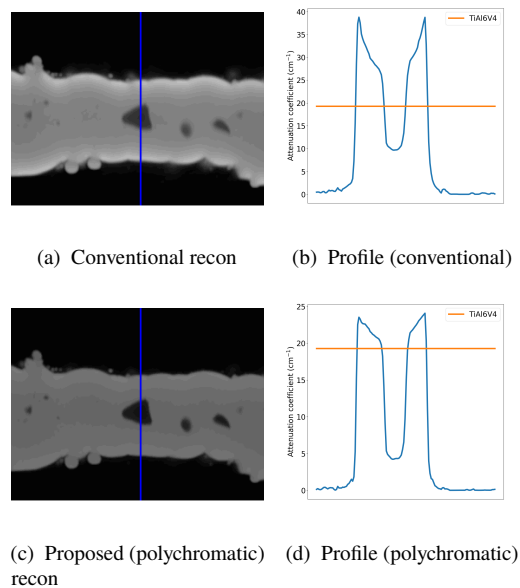(c) Proposed (polychromatic) recon   (d) Profile (polychromatic)

Fig. 7. Horizontal slices through the 3D tomographic reconstruction of experimental data for titanium alloy at 31keV. (a) and (c) show the reconstructed images, (b) and (d) show the line profile through the blue line marked in the images. (a-b) conventional recon; (c-d) proposed (polychromatic) recon using simplification I. The expected attenuation (NIST-XCOM attenuation values at 31keV) is given as the orange and green lines in the line profile.

4.3. Experimental Analysis and Discussion

We observe a clear improvement in the reconstructions that utilise beam-hardening correction. For the marble and aluminium rods (Fig. 6), the constant density assumption (simplification V) is used in the reconstruction. Here the difference between the tomogram reconstructed with the proposed method (Fig. 6c) and the tomogram from conventional reconstruction (Fig. 6a) is particularly striking. In the slice reconstructed with a monochromatic model, beam hardening changes the attenuation values reconstructed and causes the attenuation of the two materials blend together. Whereas in the slice reconstructed with a polychromatic model, the values for the attenuation coefficient inside each material are more consistent; the two materials can now be distinguished and segmented by setting thresholds (Fig. 6c). The streaking artefacts seen between the two rods in the uncorrected tomogram are significantly reduced while still present in the corrected tomogam. The attenuation coefficient of Al corresponded to the expected NIST-XCOM values at the mean X-ray energy of 46keV, however, the attenuation for marble was lower than expected. This could be due to porosity in the marble, inclusions of a lower atomic number, or a poor fit of the AM attenuation model to that for marble.

For the titanium sample (Fig. 7), the correction method uses the photoelectric absorption only assumption (simplification I). The relatively high atomic number of titanium means that photoelectric absorption, Φ, is the main attenuation mechanism over the energy range of the X-ray spectrum used (10-60keV). The Compton scattering component, Θ, is negligible in this energy range, at 40keV $\Phi = 10\Theta$ and it is not until $\tilde{9}5$keV that $\Phi = \Theta$. The excellent fit of the AM attenuation model and this photoelectric absorption only simplification with the NIST-XCOM data for Ti can be seen in Fig. 8a. The photoelectric component, given by the green line, matches closely the actual attenuation given by the blue '+' symbols.

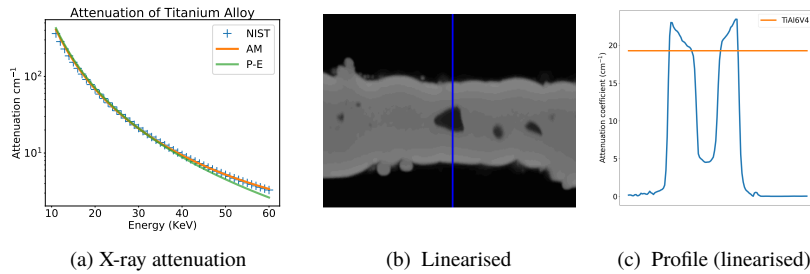(a) X-ray attenuation   (b) Linearised   (c) Profile (linearised)

Fig. 8. (a) Comparison of the energy dependence of X-ray attenuation for Ti6Al4V modelled by NIST-XCOM, Alvarez-Macovski, and proposed simplification I. (b) conventional recon from projected attenuation after *linearisation* according to the NIST-XCOM model. (c) profile through the blue line marked in image (b).

We observe the following in Fig. 7: (i) the cupping effect present in the slice of the conventional reconstruction (Fig. 7a), has been substantially corrected by the proposed method using a polychromatic model (Fig. 7c); (ii) the reconstructed attenuation coefficients are much closer to the expected NIST-XCOM values for Ti6Al4V at the mean X-ray energy 31keV; and (iii) the reconstructed attenuation coefficients in the internal voids are closer to background levels.

However, the result does not seem to have corrected the artefacts as well as expected and is not quantitative. To confirm that the algorithm was performing as designed, we also carried out conventional reconstruction on the projected attenuation data that were corrected by *linearisation*. The linearisation curve was computed directly from the NIST-XCOM X-ray attenuation data for Ti6Al4V. Both the reconstructed image (Fig. 8b) and the line profile (Fig. 7d) are similar to the results using the proposed method. While there is uncertainty about the spectrum, we are fairly confident about it due to the validation from the Amptek detector mentioned earlier. Although the effects of X-ray scatter could explain these results, we see in the example raw experiment data presented in Fig. 9, that X-ray counts beside the object are no higher than the clearfield counts. This indicates no appreciable amount of X-rays scattered from the object are being detected. Closer inspection of this raw experimental data reveals a bright, circular aberration in both the clearfield (Fig. 9a) and radiograph (Fig. 9b). This is characteristic of a secondary source of radiation emitted from transmission-type X-ray tubes. It is generated by electrons interacting with the tube housing material [38]. This secondary radiation acts as a large source blurring the system point-spread-function (PSF) and has an unknown spectrum. Line profiles included in Fig. 9c, show a broader PSF closer to the circular aberration (most easily seen comparing the circled regions). The residual cupping effects seen in the results from the both the proposed method (Fig. 7d) and using linearisation (Fig. 8c) could be explained if the unknown spectrum is softer than the spectrum assumed in reconstruction.

5. Conclusions and future research

We have produced a robust technique to model and account for X-ray beam-hardening in tomographic reconstruction. The proposed method puts a polychromatic projection operator into existing iterative reconstruction algorithms and is compatible with existing techniques which speed up reconstruction such as ordered subsets and multi-grid. The polychromatic operator is constructed from the Alvarez-Macovski (AM) X-ray attenuation model combined with a few simple assumptions about the object's material properties. The polychromatic operator has been implemented and proved to be computationally feasible in reconstructions of large datasets on the order of 100GVx used in materials science.

We have demonstrated by simulations and experiment that the method is capable of qualitatively

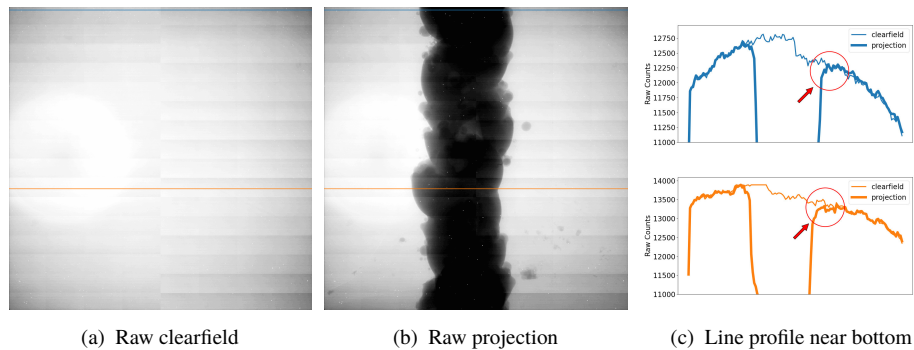| (a) Raw clearfield | (b) Raw projection | (c) Line profile near bottom |

Fig. 9. Raw data taken from the Titanium scan. Figure 9a is the clearfield, Figure 9b is the projection. The two line profiles are shown in Figures 9c. The second source is visible as a increase in intensity in the bottom centre of both the clearfield and the projection.

improving the tomographic reconstructions with beam hardening artefacts using knowledge of the X-ray spectrum. Assuming more detailed material information is known (and the effects of other non-ideal X-ray interactions, such as scatter and secondary radiation are minimal), a quantitative reconstruction of the image can be attempted. The reconstructed X-ray attenuation pixels/voxel values represent the exact attenuation value of the object at a specified energy.

We believe quantitative tomographic reconstruction is an important objective of XCT. From the results herein, performance of the simplification schemes applied to the experimental data did not reach the level of quantitative accuracy of the simulations; this is a matter deserving further investigation. There are several possibilities, involving the accuracy of the spectrum, the importance of the absorption edge contributions to the attenuation of the material (not characterised by the AM model), and other non-ideal X-ray interactions with the object not incorporated into the model such as X-ray scattering and the generation of X-ray flourescence.

The major obstacle in adopting this specific technique is the need to manually select an appropriate assumption about object properties and then enter the required material information to operate the AM model. It may be possible to automate the selection of the optimal assumption and appropriate parameter values using trial reconstructions at lower resolutions; a suitable metric must be developed to quantify performance in beam-hardening correction and is the subject of on-going research.

Funding

Disclosure

The authors declare no conflicts of interest.

References

1. J. Hsieh, B. Nett, Z. Yu, K. Sauer, J.-B. Thibault, and C. A. Bouman, "Recent Advances in CT Image Reconstruction," Curr. Radiol. Reports **1**, 39–51 (2013).
2. X. Pan, J. Siewerdsen, P. J. La Riviere, and W. A. Kalender, "Anniversary Paper: Development of x-ray computed tomography: The role of Medical Physics and AAPM from the 1970s to present," Med. Phys. **35**, 3728–3739 (2008).
3. R. A. Brooks and G. D. Chiro, "Beam hardening in X-ray reconstructive tomography," Phys. Medicine & Biol. **21**, 390 (1976).

4. A. J. Duerinckx and A. Macovski, "Polychromatic Streak Artifacts in Computed Tomography Images," J. Comput. Assist. Tomogr. **2**, 481 (1978).

5. B. D. Man, J. Nuyts, P. Dupont, G. Marchal, and P. Suetens, "Metal streak artifacts in X-ray computed tomography: a simulation study," IEEE Transactions on Nucl. Sci. **46**, 691–696 (1999).

6. S. W. Young, H. H. Muller, and W. H. Marshall, "Computed tomography: beam hardening and environmental density artifact." Radiology **148**, 279–283 (1983).

7. L. A. Feldkamp, L. C. Davis, and J. W. Kress, "Practical cone-beam algorithm," JOSA A **1**, 612–619 (1984).

8. P. Gilbert, "Iterative methods for the three-dimensional reconstruction of an object from projections," J. Theor. Biol. **36**, 105–117 (1972).

9. G. R. Davis and F. S. Wong, "X-ray microtomography of bones and teeth," Physiol. measurement **17**, 121 (1996).

10. A. N. Golab, M. A. Knackstedt, H. Averdunk, T. Senden, A. R. Butcher, and P. Jaime, "3d porosity and mineralogy characterization in tight gas sandstones," The Lead. Edge **29**, 1476–1483 (2010).

11. W. D. McDavid, R. G. Waggener, W. H. Payne, and M. J. Dennis, "Correction for spectral artifacts in cross-sectional reconstruction from x rays," Med. Phys. **4**, 54–57 (1998).

12. S. C. Pang and S. Genna, "Corrections for X-Ray Polychromaticity Effects on Three-Dimensional Reconstruction," IEEE Transactions on Nucl. Sci. **23**, 623–626 (1976).

13. G. T. Herman, "Correction for beam hardening in computed tomography," Phys. Medicine & Biol. **24**, 81 (1979).

14. D. D. Robertson and H. K. Huang, "Quantitative bone measurements using x-ray computed tomography with second-order correction," Med. Phys. **13**, 474–479 (1998).

15. A. J. Burghardt, G. J. Kazakia, A. Laib, and S. Majumdar, "Quantitative assessment of bone tissue mineralization with polychromatic micro-computed tomography," Calcif. tissue international **83**, 129 (2008).

16. E. V. de Casteele, D. V. Dyck, J. Sijbers, and E. Raman, "An energy-based beam hardening model in tomography," Phys. Medicine Biol. **47**, 4181–4190 (2002).

17. M. Krumm, S. Kasperl, and M. Franz, "Reducing non-linear artifacts of multi-material objects in industrial 3d computed tomography," NDT & E Int. **41**, 242–251 (2008).

18. A. N. Z. Evershed, D. Mills, and G. Davis, "Multi-species beam hardening calibration device for x-ray microtomography," in *Developments in X-Ray Tomography VIII,* vol. 8506 (International Society for Optics and Photonics, 2012), p. 85061N.

19. R. E. Alvarez and A. Macovski, "Energy-selective reconstructions in X-ray computerised tomography," Phys. Medicine & Biol. **21**, 733 (1976).

20. G. Christ, "Exact treatment of the dual-energy method in CT using polyenergetic x-ray spectra," Phys. Medicine & Biol. **29**, 1501 (1984).

21. T. Xia, A. M. Alessio, and P. E. Kinahan, "Dual energy CT for attenuation correction with PET/CT," Med. Phys. **41**, 012501 (2014).

22. B. D. Man, J. Nuyts, P. Dupont, G. Marchal, and P. Suetens, "An iterative maximum-likelihood polychromatic algorithm for CT," IEEE Transactions on Med. Imaging **20**, 999–1008 (2001).

23. G. Van Gompel, K. Van Slambrouck, M. Defrise, K. J. Batenburg, J. de Mey, J. Sijbers, and J. Nuyts, "Iterative correction of beam hardening artifacts in CT: Iterative correction of beam hardening artifacts in CT," Med. Phys. **38**, S36–S49 (2011).

24. J. A. Fessler, E. P. Ficaro, N. H. Clinthorne, and K. Lange, "Grouped-coordinate ascent algorithms for penalized-likelihood transmission image reconstruction," IEEE transactions on medical imaging **16**, 166–175 (1997).

25. G. V. Gompel, K. V. Slambrouck, M. Defrise, K. J. Batenburg, J. d. Mey, J. Sijbers, and J. Nuyts, "Iterative correction of beam hardening artifacts in CT," Med. Phys. **38**, S36–S49 (2011).

26. S. Tilley, W. Zbijewski, and J. W. Stayman, "Model-based material decomposition with a penalized nonlinear least-squares CT reconstruction algorithm," Phys. Medicine & Biol. **64**, 035005 (2019). Publisher: IOP Publishing.

27. L. Brabant, E. Pauwels, M. Dierick, D. V. Loo, M. A. Boone, and L. V. Hoorebeke, "A Novel Beam Hardening Correction Method Requiring No Prior Knowledge, Incorporated in an Iterative Reconstruction Algorithm," NDT & E Int. **51**, 68–73 (2012).

28. R. Gordon, R. Bender, and G. T. Herman, "Algebraic Reconstruction Techniques (ART) for three-dimensional electron microscopy and X-ray photography," J. Theor. Biol. **29**, 471–481 (1970).

29. A. H. Anderson and A. C. Kak, "Simultaneous Algebraic Reconstruction Technique (SART): A superior implementation of the ART algorithm," Ultrason. Imaging **6**, 81–94 (1984).

30. K. Lange and R. Carson, "EM reconstruction algorithms for emission and transmission tomography," J. Comput. Assist. Tomogr. **8**, 306–316 (1984).

31. Beer, "Bestimmung der absorption des rothen lichts in farbigen flüssigkeiten," Annalen der Physik und Chemie. **86**, 78–88 (1760).

32. O. Klein and Y. Nishina, "The Scattering of Light by Free Electrons according to Dirac's New Relativistic Dynamics," Nature **122**, 398–399 (1928).

33. M. Paziresh, A. M. Kingston, S. J. Latham, W. K. Fullagar, and G. M. Myers, "Tomography of Atomic Number and Density of Materials Using Dual-Energy Imaging and the Alvarez and Macovski Attenuation Model," J. Appl. Phys. **119**, 214901 (2016).

34. M. J. Berger, J. H. Hubbell, S. M. Seltzer, J. Chang, J. S. Coursey, R. Sukumar, D. Zucker, and K. Olsen, "XCOM: Photon Cross Section Database," (2010).

35. A. M. Kingston, G. R. Myers, S. J. Latham, B. Recur, H. Li, and A. P. Sheppard, "Space-filling x-ray source trajectories for efficient scanning in large-angle cone-beam computed tomography," IEEE Transactions on Comput. Imaging **4**, 447–458 (2018).
36. G. R. Myers, A. M. Kingston, S. J. Latham, B. Recur, T. Li, M. L. Turner, L. Beeching, and A. P. Sheppard, "Rapidly converging multigrid reconstruction of cone-beam tomographic data," in *Developments in X-Ray Tomography X,* vol. 9967 (International Society for Optics and Photonics, 2016), p. 99671M.
37. G. R. Myers, S. J. Latham, A. M. Kingston, J. Kolomazník, V. Krajíček, T. Krupka, T. K. Varslot, and A. P. Sheppard, "High cone-angle x-ray computed micro-tomography with 186 gigavoxel datasets," in *Developments in X-Ray Tomography X,* vol. 9967 (International Society for Optics and Photonics, 2016), p. 99670U.
38. M. N. Boone, J. Vlassenbroeck, S. Peetermans, D. Van Loo, M. Dierick, and L. Van Hoorebeke, "Secondary radiation in transmission-type x-ray tubes: simulation, practical issues and solution in the context of x-ray microtomography," Nucl. Instruments Methods Phys. Res. Sect. A: Accel. Spectrometers, Detect. Assoc. Equip. **661**, 7–12 (2012).